

Supplementary Information

Nano-flocks of bimetallic organic framework for efficient hydrogen evolution electrocatalysis

Mohd. Khalid,*^a Ayaz Hassan,^a Ana M.B. Honorato,^b Frank N. Crespilho,^a Hamilton Varela*^a

^a Institute of Chemistry of São Carlos, University of São Paulo, POBox 780, 13560-970, São Carlos, SP, Brazil.

^b Center of Advanced Science and Engineering for Carbon (Case4carbon), Department of Macromolecular Science and Engineering, Case Western Reserve University, 10900 Euclid Avenue, Cleveland, OH 44106, USA.

Chemicals and materials

Nickel(II) acetate tetrahydrate ($\text{NiO}_4\text{C}_4\text{H}_6 \cdot 4\text{H}_2\text{O}$; 99.0%), Cobalt(II) nitrate hexahydrate ($\text{Co}(\text{NO}_3)_2 \cdot 6\text{H}_2\text{O}$; >99.0%), 2, 6-naphthalene dicarboxylic acid dipotassium salt (95.0%), potassium hydroxide (KOH, 99%) and platinum carbon black (Pt/C, 20 wt. %) were purchased from Sigma-Aldrich and used as received without further purification. Nebulizer machine was purchased from the medical store. Nebulizer compressor is a drug delivery device used to administer medication in the form of a mist inhaled into lungs, which works according to Bernoulli's principle. Deionized water with a resistivity of $18.25\text{ M}\Omega\text{ cm}^{-1}$ used throughout the experiments was purified with a water purification cation exchange system (Milli-Q Advantage A10, Merck Millipore, USA).

Synthesis of graphene oxide (GO)

GO was synthesized by the oxidation of graphite powder according to the Hummers' method, as reported elsewhere [S1]. In a typical synthesis process, 5 g commercial expanded graphite (50 μm , EC1000) and 15 g potassium permanganate were initially mixed in a round-bottom flask (500 ml) with ice-water bath. Then 100 mL of concentrated sulfuric acid (98%) was added to the mixture with continuous stirring until a uniform liquid paste was formed. Afterward, the water bath was removed and stirring was kept continuous until a foam-like intermediate formed with a large volumetric expansion. Then 400 mL of deionized water was added. After 1-hour continuous stirring at 80° C, a homogeneous dark brown suspension was obtained. Then 50 mL of H₂O₂ (30 wt. %) was slowly added to the mixture and the color of the suspension was changed from dark brown to yellow. The suspension was then filtered and subjected to repeated washing with 1 M HCl solution and deionized water, followed by centrifuging at 10,000 rpm to remove impurities and finally the solution was dialyzed in a dialysis bag (dialysis tubing benzoylated, D7884-1FT, Sigma-Aldrich) for 15 days. After drying the GO dispersion at 50 °C under vacuum for 48 h, the powder of GO was obtained. Then, 2 mg mL⁻¹ of GO dispersion was prepared in the double distilled water.

NiCo-MOF nano-flocks grown on Ni-mesh

Firstly, a piece of Ni-mesh, wire diameter about 60 μm , as a substrate was rubbed by coarse sand paper to create some roughness on the substrate and washed with ethanol and water. Afterward, the piece of Ni-mesh immersed into 20 mL solution of methanol and water (1:3) containing 20 mg organic linker (2,6-naphthalene dicarboxylic acid dipotassium salt), so that the organic ligand can be absorbed onto the surface of Ni-mesh through Vander-Waals forces and electrostatic interactions. Then, the cobalt nitrate (5 mg) and nickel acetate (15 mg) salts in the ratio of 1:3 was loaded into the mixture and left overnight at 50 ° C, which resulted successful growth of nano-flocks of NiCo-MOF onto the Ni-mesh. We also examined the morphological structure of the obtained materials by varying the ratio of cobalt nitrate and nickel acetate (1:1), while keeping the same amount (20 mg) of organic linker same, we found that this ratio could not produce nano-flocks and resulted nonuniform nano-rod type structure of MOF and agglomerated particles on the substrate. This may be because of the higher amount of the cobalt nitrate generally accounts for faster nucleation rate and hence agglomeration occurred, as can be seen in Fig. 1S.

Physical characterizations

The morphological characterization of the materials was investigated with ZEISS-Gemini scanning electron microscopy (SEM). High-resolution transmission electron microscopy (HERTEM) images of the samples was obtained using a JEM2100 LaB₆ 200 kV transmission electron microscope and elemental composition was acquired with accelerating voltage of 200 kV. For obtaining HRTEM images, the catalyst was dispersed in isopropanol by using ultrasonication for one minute and a single drop took out with the help of micropipette and coated onto the carbon-film copper grids (EMS, 400 mesh). The TEM-EDS elemental mapping was taken with an accelerating voltage of 40 kV. The XRD patterns were recorded using a Bruker D8-advance X-ray powder diffractometer with Cu K α radiation source ($\lambda = 1.54 \text{ \AA}$); data was collected for 2θ values between 5 to 80° at a rate of 0.075° s⁻¹. X-ray photoelectron spectroscopy (XPS) measurements were carried out on a PHI-5300, ESCA spectrometer (PerkinElmer) using 300W Al K α radiation. Brunaur-Emmett-Teller (BET) surface area was analyzed by N₂ adsorption desorption measurements using Micromeritics Auto Chem. 2920 instrument.

Microscopic Fourier transform infrared (FTIR) spectroscopy in the mid region of the as-prepared samples was performed using FTIR microscope (Hyperion 3000). The spectra were recorded in the reflectance mode, using a gold mirror upon which the sample were fixed using a scotch tape. A spectral resolution of 4 cm⁻¹ and 64 scans were co-added in the 4000-900 cm⁻¹ spectral window using liquid N₂ cooled 64 x 64 elements focal plane array (FPA) detector. All the FTIR spectra shown here are the difference spectra, where the absorption signals corresponding to the background are subtracted from those of the samples. FTIR chemical images were collected using the same detector. Each element of the FPA works as an individual detector, making possible the measurement of a full spectrum from a single point with a spatial resolution of 2.7 μm . One single FTIR image is thus a collection of 4,096 spectra, obtained just in two minutes. In this technique, the absorption band corresponding to the characteristic functional group is integrated, which results in the formation of color coded image, where the blue color shows the lowest concentration and the red color shows the highest concentration. FTIR spectra and images of the samples were recorded in order to attribute their spectral bands and thus determine their chemical distribution in the specific sample.

Electrochemical measurements

The electrocatalytic activity of the catalysts was performed using Autolab electrochemical workstation in three-electrode cell configuration. All electrochemical experiments were carried out in Ar-saturated 0.1 M KOH electrolyte at room temperature of *ca.* 25 °C. The Hg/HgO (0.1 M KOH filling solution) and graphite rod were used as reference and counter electrodes, respectively. The current density was normalized by assuming the geometrical area (0.7 cm²) as flat of the Ni-mesh. All data was acquired without *iR*-corrections. The ink of Pt/C (20 wt. %) was prepared using 5 mg of the catalyst, 1 mL of ethanol and 20 μL of a 5 wt. % Nafion solution and ultrasonicated for 30 min for homogeneous mixing and then Ni-mesh was dipped into the ink and kept under vacuum for further use. All the potentials were calibrated and converted to reversible hydrogen electrode, scale by adding a value of 0.926 V, according to the equation, $E_{vs\ RHE} = E_{vs\ Hg/HgO} + 0.095 + 0.059pH$. The linear sweep voltammogram for the OER evolution was recorded at scan rate of 5 mV s⁻¹ after purging Argon gas for 30 min in 0.1 M KOH electrolyte.

Table 1 Tentative vibrational modes assignment of the various functional groups observed in the infrared spectra of the samples.

NiCo-MOF (Peak position, cm ⁻¹)	NiCo-MOF/rGOAS (Peak position, cm ⁻¹)	Assignment
	1674	C=O stretching
	1640	O-H bending
1601	1601	C=C stretching of aromatic ring
	1554	C-C stretching
1544		C-C stretching
1494	1494	Aromatic ring vibration
1479	1479	C-C stretching, C-H bending
	1415	
1404		C-H bending
	1399	
1393		C-C stretching, C-H bending
1355	1357	Ring deformation
	1296	C-C bending
1192	1192	C-H bending

Table 2 Comparison of exchange current densities, overpotentials, and Tafel slop values with several recently reported HER electrocatalysts.

Catalysts	Electrolyte	Exchange current density (j_o , mA/cm ²)	j_{10} (V) vs. RHE	Tafel slop (mV dec ⁻¹)	References
NiCo-MOF/GOAS	0.1 M KOH	$\log j_o = 0.880$ $j_o = 0.132$	0.210	73	This work
CoPS (100) CoPS (111)	0.5 M H ₂ SO ₄	0.0387 0.0047	0.260 0.285	109 186	S2
Fe ₂ P@rGO	0.5 M H ₂ SO ₄	0.146	0.101	55.2	S3
double-gyroid, MoS ₂ /FTO	0.5 M H ₂ SO ₄	6.9×10^{-4}	0.300	50	S4
MoS _x /NCNT	0.5 M H ₂ SO ₄	3.31×10^{-2}	0.110	40	S5
CoSe ₂ NP/CP	0.5 M H ₂ SO ₄	$(4.9 \pm 1.4) \times 10^{-3}$	0.180 j_{100}	42.1	S6
CoS ₂ NW/Graphite	0.5 M H ₂ SO ₄	2.8×10^{-3}	0.145	51.6	S7
NiMoN _x /C	0.1 HClO ₄	0.24	-	35.9	S8
Co _{0.6} Mo _{1.4} N ₂	0.1 HClO ₄	0.23	0.200	-	S9
Ni ₂ P hollow NPs/Ti	0.5 M H ₂ SO ₄	3.3×10^{-2}	0.100	46	S10
CoP/Ti	0.5 M H ₂ SO ₄	0.14	0.075	50	S11
CoPS NP/S	0.5 M H ₂ SO ₄	0.984	0.048	56	S12
Interconnected network MoP/S	0.5 M H ₂ SO ₄	0.086	0.150	54	S13
Pt-Ni-Co	0.1 M KOH	0.900	0.022 j_5	-	S14
Co ₂ P nanorods	0.5 M H ₂ SO ₄	0.025	0.134	51.7	S15
MoS ₂ @Ni/Carbon cloth	1 M KOH	0.807	0.091	89	S16
Pt/Au/C	0.1 M KOH	0.700	-	-	S17
Pt/Cu nanowires	0.1 M KOH	2.10	0.013 j_5	-	S18
MoS ₂ /Pd	0.5 H ₂ SO ₄	805 μ A	0.078	89	S19
Metallic WO ₂ carbon	0.5 H ₂ SO ₄	0.64	0.058	46	S20
Ni-Fe-P	1 M KOH	0.251	0.142	84.24	S21
C@NiCoP	0.5 H ₂ SO ₄	0.21	0.076	43	S22
CoO.4Fe0.6 LDH/g-CN _x Co(OH) ₂ /g-CN _x Fe(OH) ₂ /g-CN _x	1M KOH 1M KOH 1M KOH	0.157 ± 0.003 0.015 ± 0.008 0.051 ± 0.005	0.270 ± 0.008 0.586 ± 0.01 0.489 ± 0.005	79 ± 3 165 ± 6 136 ± 8	S23

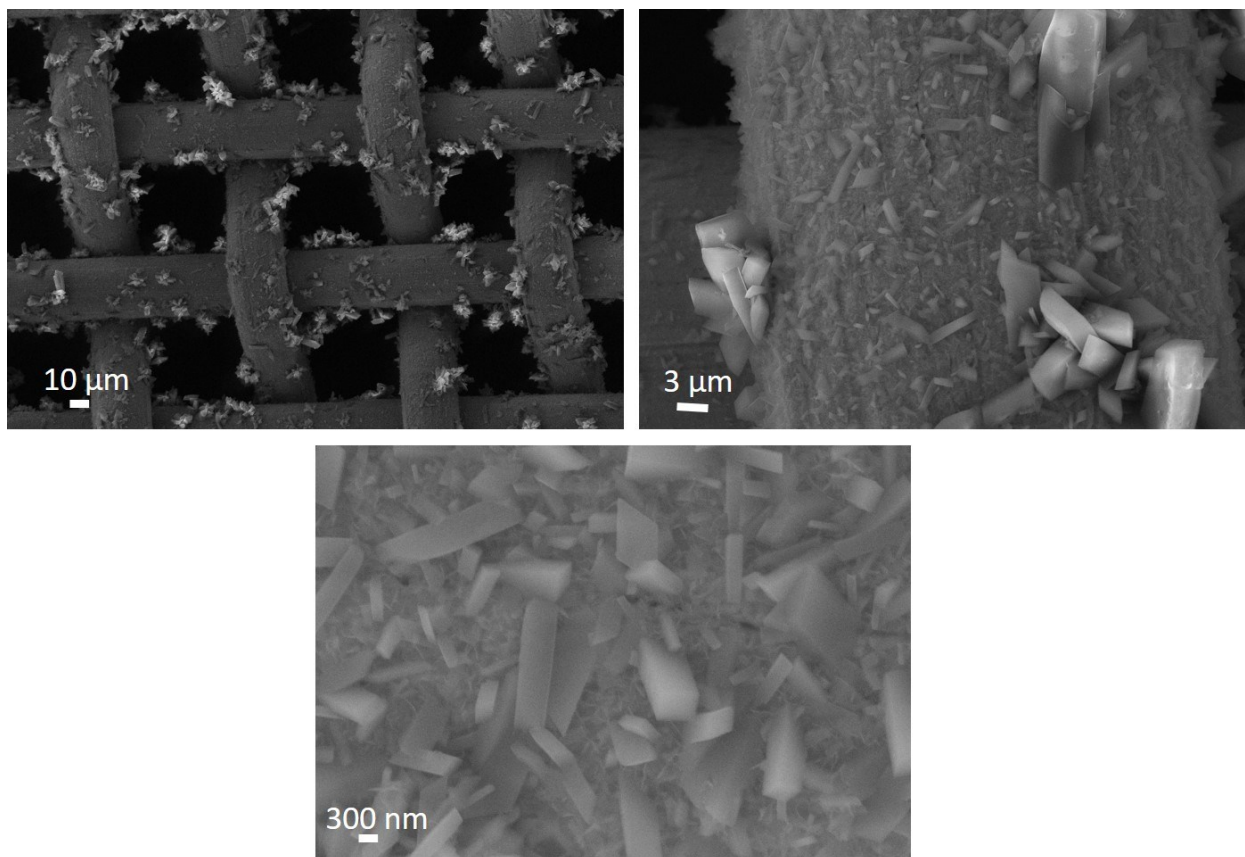


Fig. 1S SEM images of NiCo-MOF crystals at different magnifications with Ni and Co ratio of 1:1.

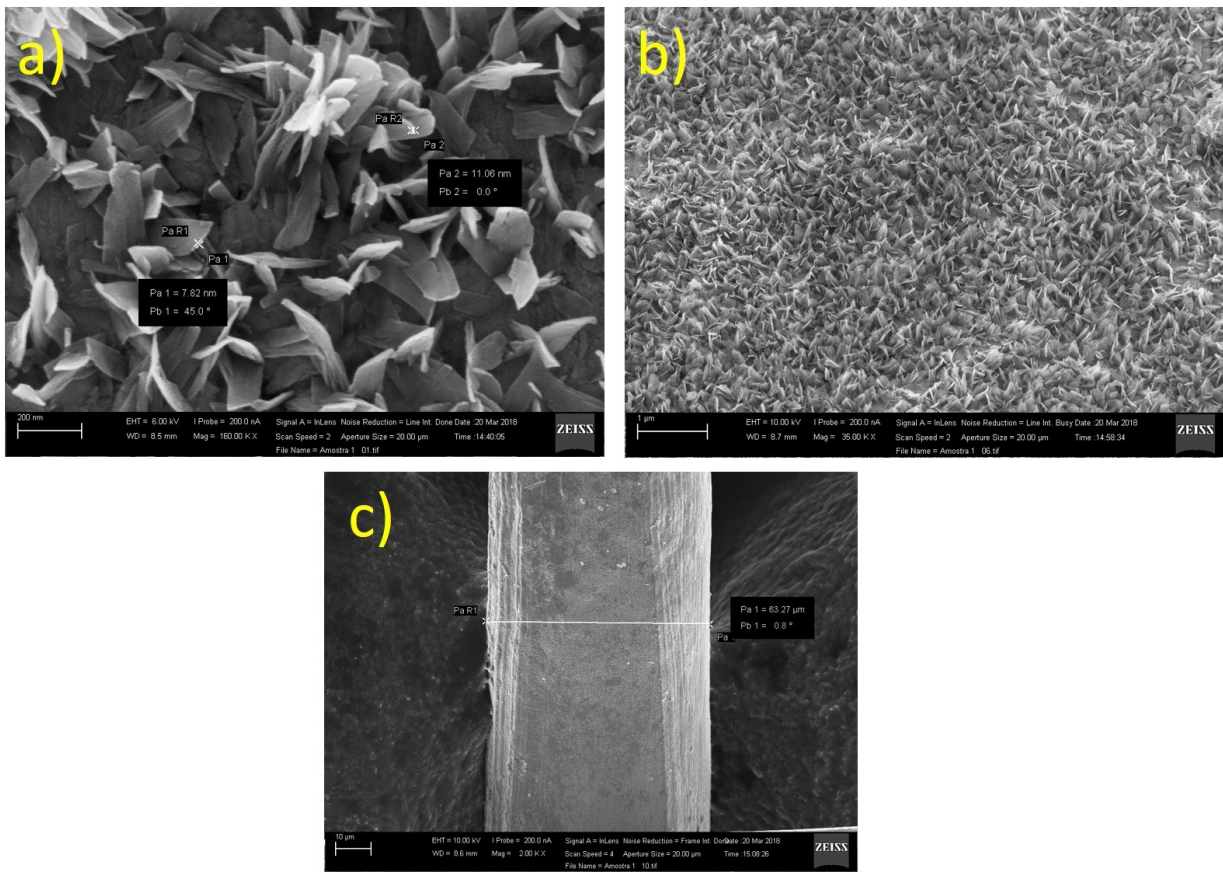


Fig. 2S SEM images of NiCo-MOF nano-flocks with Co and Ni ratio of 1:3.

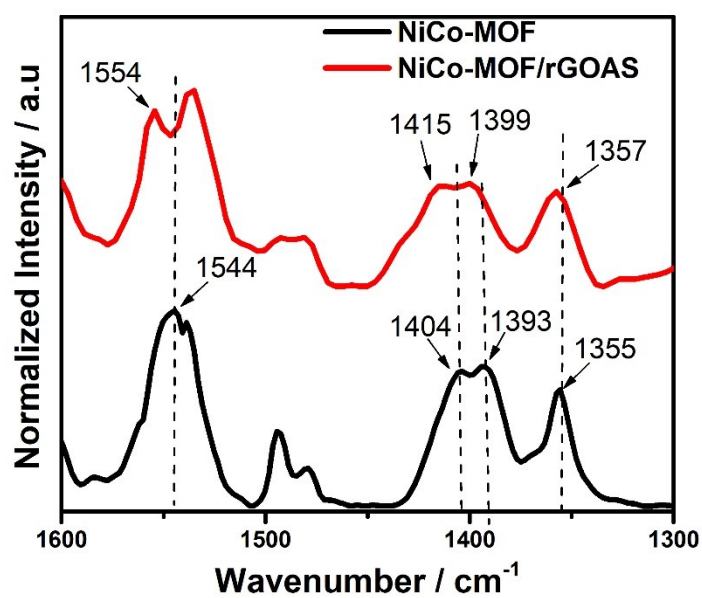


Fig. 3S Microscopic-FTIR spectra showing upward shifts of several spectral bands.

In addition, a minor shift was also observed in the band ca. 1355 cm⁻¹ of NiCO-MOF, which is upward shifted to 1357 cm⁻¹ for NiCo-MOF/rGOAS.

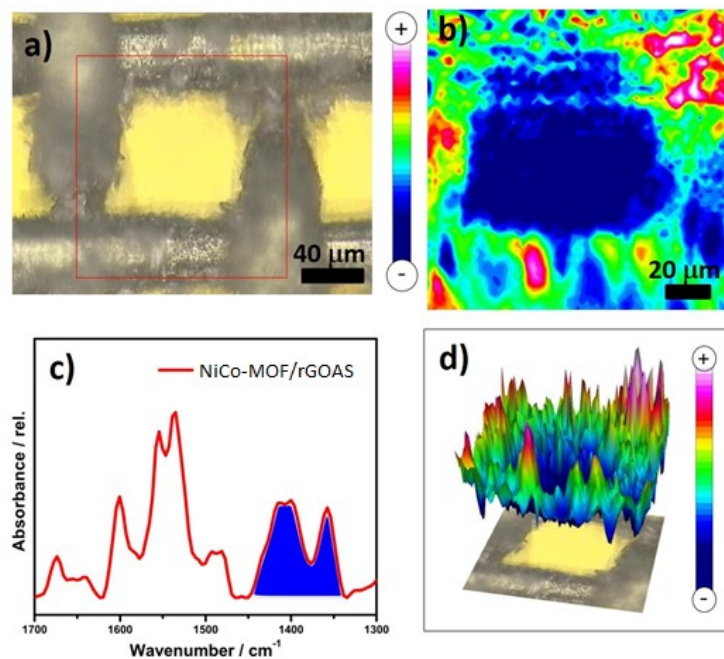


Fig. 4S a) Optical image showing a part of the Ni mesh covered with the catalyst. The area marked in red is selected for the extraction of the spectra and consequent chemical images, b) 2D Chemical image showing the distribution of spectral bands at 1405, 1390 and 1356 cm⁻¹, c) FTIR spectrum of NiCo-MOF/GOAS, with the integrated spectral bands highlighted in blue and d) 3D chemical image.

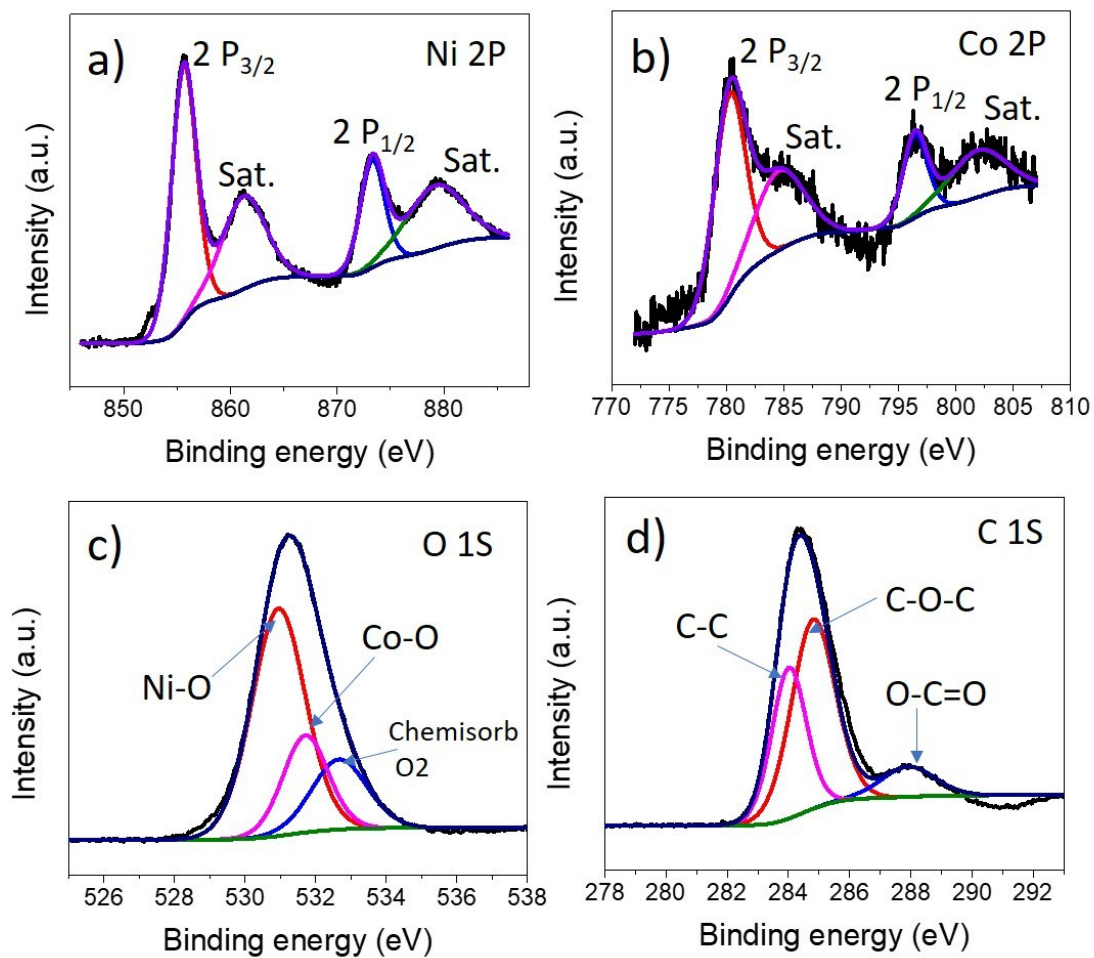


Fig. 5S XPS analysis of NiCo-MOF/GOAS. a) HR-XPS of Ni 2p, b) HR-XPS of Co 2p, c) HR-XPS of O 1s and d) HR-XPS of C 1s.

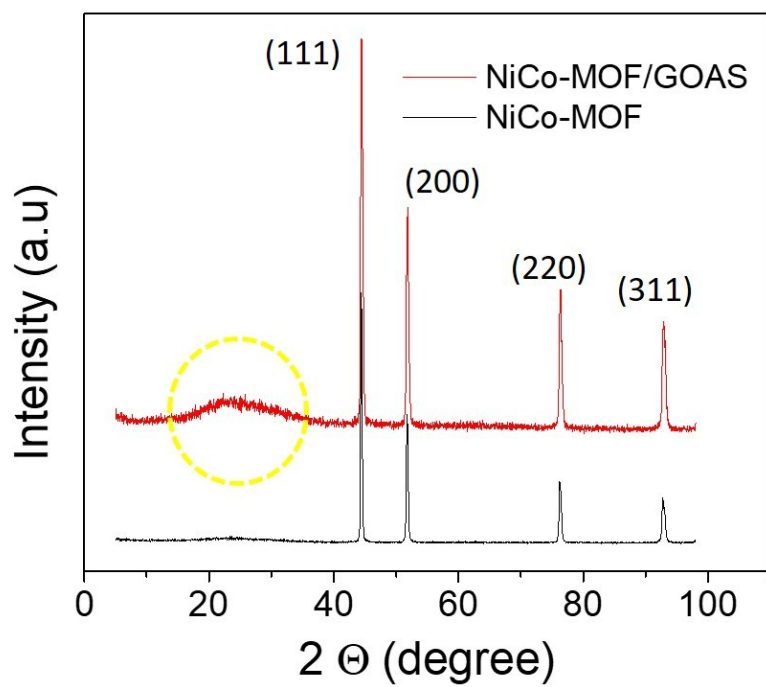


Fig. 6S XRD pattern of NiCo-MOF and NiCo-MOF/GOAS.

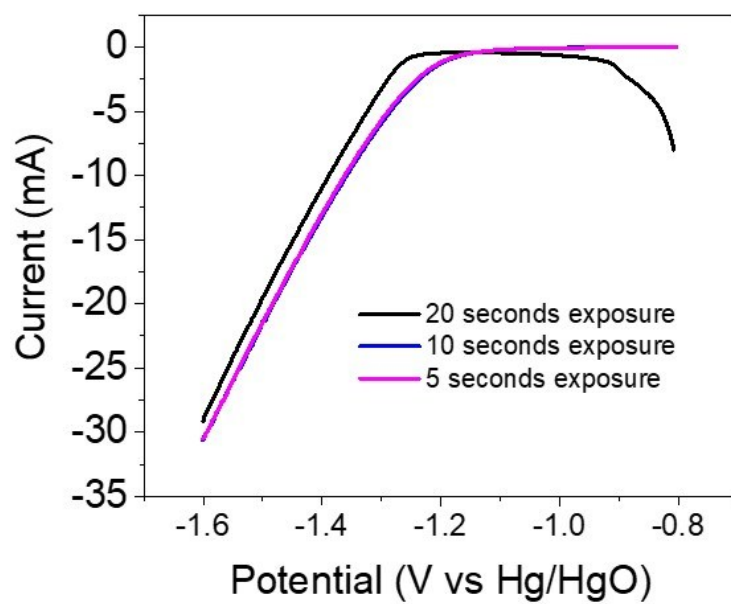


Fig. 7S Different time exposure of GOAS onto the NiCo-NMOF catalysts and their HER performance in 0.1 M KOH at 5 mV s⁻¹.

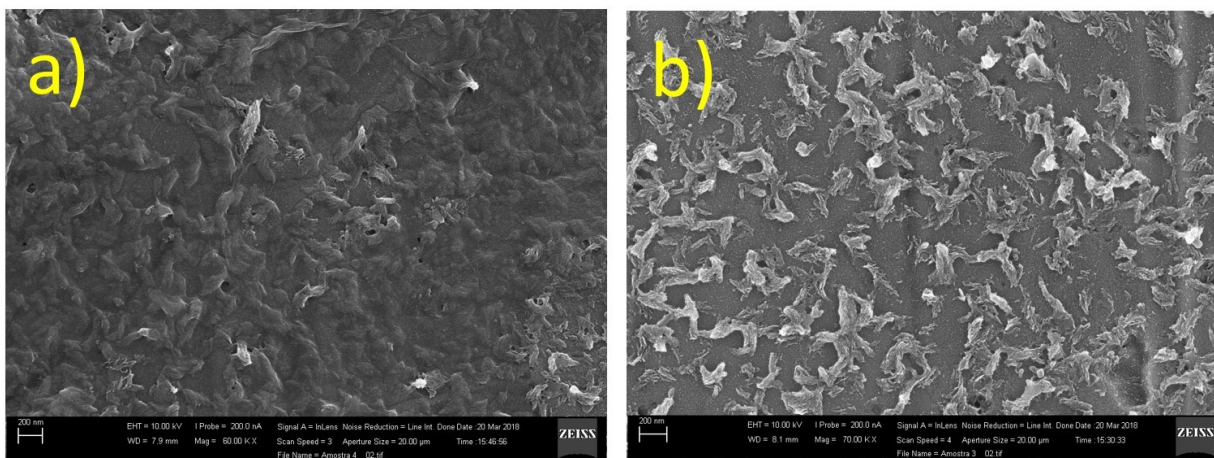


Fig. 8S a) SEM image NiCo-MOF/GOAS and b) SEM image of NiCo-MOF after chronoamperometric operation.

Electrochemical active surface area. In order to characterize the electrochemically active surface area (ECSA) of the catalysts, we quantified the electrical double layer capacitance of the electrodes. For this, we recorded the cyclic voltammogram (CV) at various scan rates from 5 to 20 mV s⁻¹ in the potential region of -0.12 to 0, in the non-faradic region, as displayed in the Figures below. Usually, the qualitatively larger CV indicates the higher electrical double layer capacitance (C_{dl}) of the electrode and is a reliable indicator of ECSA when the catalyst has excellent electronic conductivity. The C_{dl} of the electrode was estimated by plotting the charging current density differences $\Delta j = j_{anodic} - j_{cathodic}$ at the potential of -0.08 V vs Hg/HgO against the scan rates. The slope of this plot was divided by 2 to obtain double layer capacitance of the electrode, according to the equation 1.

$$\text{Double layer capacitance of electrode } (C_{dl}) = \frac{1}{2} \frac{\Delta(ja - jc)}{\Delta(\text{scan rate})} \quad (\text{Eq. 1})$$

Thus, the values of C_{dl} were calculated to be 2.49 mF cm⁻² and 1.09 mF cm⁻² for NiCo-MOF/rGOAS and bare NiCo-MOF catalysts, respectively.

For the estimation of ECSA, a specific capacitance (C_s) value of 0.040 mF cm⁻² was adopted because of the C_s for a flat surface is generally found to be in the range of 0.020 - 0.060 mF cm⁻² [24-28] in alkaline medium. Thus, the ECSAs can be calculated according to the following equation 2.

$$\text{ECSA} = C_{dl}/C_s \quad (\text{Eq. 2})$$

The calculated ECSAs of NiCo-MOF/rGOAS and bare NiCo-MOF were about to be 62.25 and 27.24 cm², respectively.

Considering the higher electrochemically active surface area of the catalyst NiCo-MOF/rGO, we strongly believe that the enhanced performance of the catalyst NiCo-MOF/rGOAS is emerging from its larger ECSA as well as excellent electronic conduction between NiCo-MOF and rGOAS, which is evidenced by the EIS results.

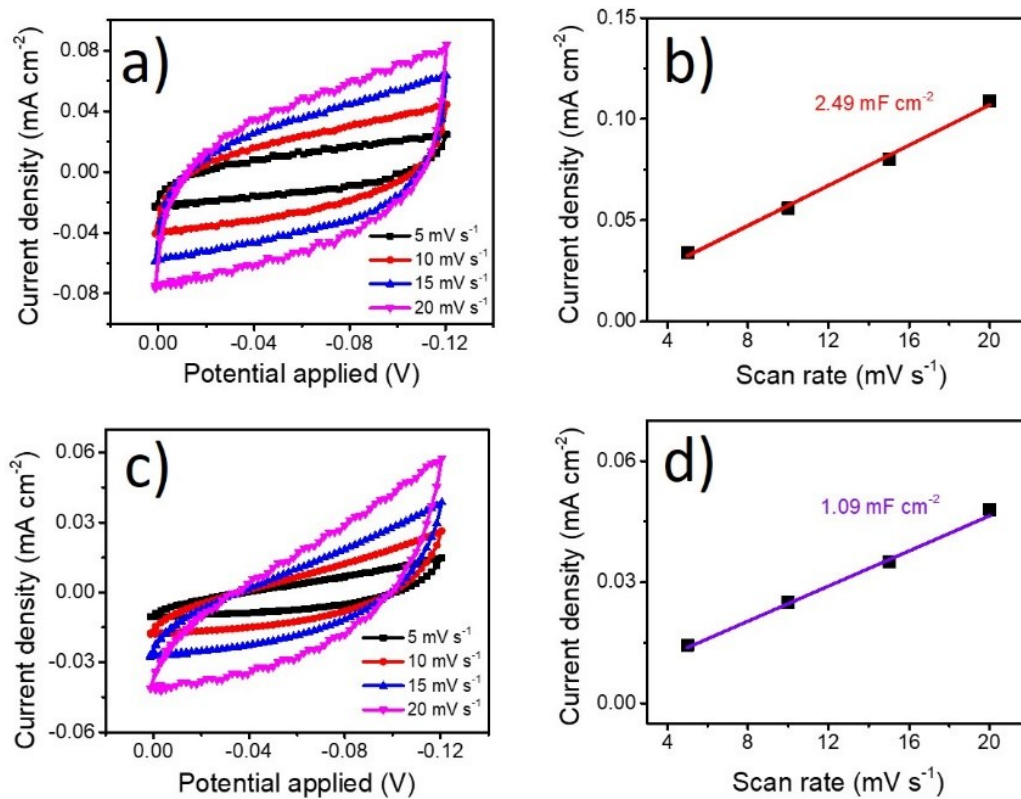


Fig. 9S Electrochemical active surface area. a) and c) CVs of NiCo-MOF-rGO and NiCo-MOF, respectively, b) and d) Charging current density differences ($\Delta j = j_a - j_b$) at an overpotential of -0.08 V plotted against scan rates fitted to linear regression enables the estimation of C_{dl} .

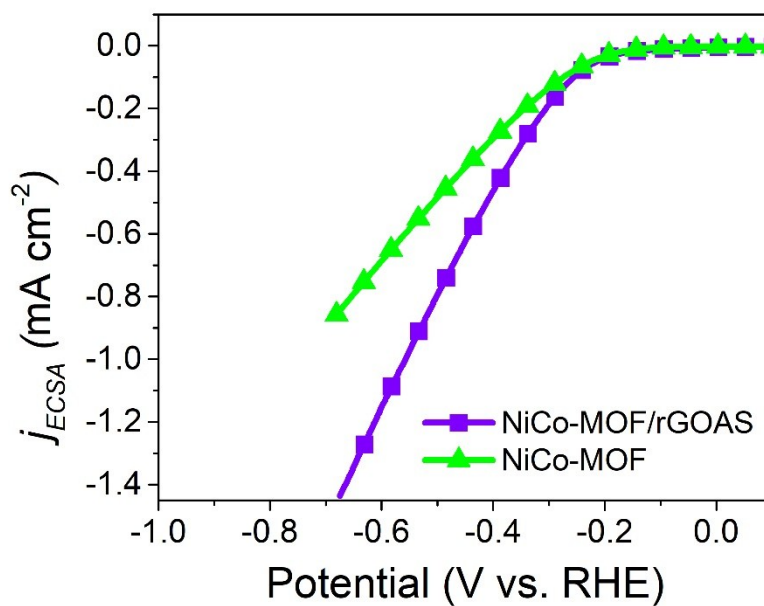


Fig. 10S ECSA normalized HER performance of NiCo-MOF/rGOAS and NiCo-MOF.

Supplementary References

- S1 Mohd. Khalid, H. Varela, *J. Mater. Chem. A*, 2018, **6**, 3141.
- S2 T. Wu, M. L. Stone, M. J. Shearer, M. J. Stolt, I. A. Guzei, R. J. Hamers, R. Lu, K. Deng, S. Jin, J. R. Schmidt, *ACS Catal.*, 2018, **8**, 1143.
- S3 M. Liu, L. Yang, T. Liu, Y. Tang, S. Luo, C. Liu, Y. Zenga, *J. Mater. Chem. A*, 2017, **5**, 8608.
- S4 J. Kibsgaard, Z. Chen, B. N. Reinecke, T. F. Jaramillo, *Nature Mater.*, 2012, **11**, 963.
- S5 D. J. Li, U. N. Maiti, J. Lim, D. S. Choi, W. J. Lee, Y. Oh, G. Y. Lee, S. O. Kim, *Nano Lett.*, 2014, **14**, 1228.

S6 D. Voiry, H. Yamaguchi, J. Li, R. Silva, D. C. B. Alves, T. Fuita, M. Chen, T. Asefa, V. B. Shenoy, G. Eda, M. Chhowalla, *Nature Mater.*, 2013, **12**, 850.

S7 D. Kong, H. Wang, Z. Lu, Y. Cui, *J. Am. Chem. Soc.*, 2014, **136**, 4897.

S8 W.-F. Chen, C.-H. Wang, K. Sasaki, N. Marinkovic, W. Xu, J. T. Muckerman, Y. Zhu, R. R. Adzic, *Energy Environ. Sci.*, 2013, **6**, 943.

S9 D. H. Youn, S. Han, J. Y. Kim, J. Y. Kim, H. Park, S. H. Choi, J. S. Lee, *ACS Nano*, 2014, **8**, 5164.

S10 W.-F. Chen, K. Sasaki, C. Ma, A. I. Frankil, N. Marinkof, J. T. Muckerman, Y. Zhu, R. R. Adzic, *Angew. Chem. Int. Ed.* 2012, **51**, 6131.

S11 E. J. Popczun, C. G. Read, C. W. Roske, N. S. Lewis, R. E. Schaak, *Angew. Chem. Int. Ed.* 2014, **126**, 5531.

S12 M. C. Acevedo, M. L. Stone, J. R. Schmidt, J. G. Thomas, Q. Ding, H.-C. Chang, M.-L. Tsai, J.-H. He, S. Jin, *Nat. Mater.*, 2015, **14**, 1245.

S13 Z. Xing, Q. Liu, A. M. Asiri, X. Sun, *Adv. Mater.*, 2014, **26**, 5702.

S14 A. Oh, Y. J. Sa, H. Hwang, H. Baik, J. Kim, B. Kim, S. H. Joo, K. Lee, *Nanoscale* 2016, **8**, 16379.

S15 Z. P. Huang, Z. Z. Chen, Z. B. Chen, C. C. Lv, M. G. Humphrey, C. Zhang, *Nano Energy* 2014, **9**, 373.

S16 Z. Xing, X. Yang, A. M. Asiri, X. Sun, *ACS Appl. Mater. Interfaces* 2016, **8**, 14521.

S17 E. G. Mahoney, W. Sheng, Y. Yan and J. G. Chen, *Chem. Electro. Chem.*, 2014, **1**, 2058.

S18 S. M. Alia, B. S. Pivovar and Y. Yan, *J. Am. Chem. Soc.*, 2013, **135**, 13473.

S19 Z. Luo, Y. Ouyang, H. Zhang, M. Xiao, J. Ge1, Z. Jiang, J. Wang, D. Tang, X. Cao, C. Liu, W. Xing, *Nat. Comm.*, 2018, **9**, 2120

- S20 R. Wu, J. F. Zhang, Y. M. Shi, D. L. Liu, B. Zhang, *J. Am. Chem. Soc.* 2015, **137**, 6983.
- S21 Z. Z. Ma, R. X. Li, M. Wang, H. J. Meng, F. Zhang, X. Q. Bao, B. Tang, X. G. Wang, *Electrochim. Acta*, 2016, **219**, 194.
- S22 Y. Bai, H. Zhang, L. Liu, H. Xu, Y. Wang, *Chem. Eur. J.* 2016, **22**, 1021.
- S23 T. Bhowmik, M. K. Kundu, S. Barman, *ACS Appl. Energy Mater.*, 2018, **1**, 1200.
- S24 Z. Fang, L. Peng, Y. Qian, X. Zhang, Y. Xie, J. J. Cha, G. Yu, *J. Am. Chem. Soc.* 2018, **140**, 5241.
- S25 J. Kibsgaard, C. Tsai, K. Chan, J. D. Benck, J. K. Nørskov, F. A. Pedersen, T. F. Jaramillo, *Energy Environ. Sci.* 2015, **8**, 3022.
- S26 B. Conway, B. Tilak, *Electrochim. Acta*, 2002, **47**, 3571.
- S27 K. Fan, H. Chen, Y. Ji, H. Huang, P. M. Claesson, Q. Daniel, B. Philippe, H. Rensmo, F. Li, Y. Luo, L. Sun, *Nat. Commun.*, 2016, **7**, 11981.
- S28 C. C. McCrory, S. Jung, J. C. Peters, T. F. Jaramillo, *J. Am. Chem. Soc.*, 2013, **135**, 16977.